Наносистеми, наноматеріали, нанотехнології
Nanosistemi, Nanomateriali, Nanotehnologii
2021, т. 19, № 2, сс. 363–373

PACS numbers: 61.05.jm, 68.37.Hk, 68.37.Lp, 78.40.-q, 78.55.Mb, 78.67.Sc, 81.70.Jb

Optoelectronic Properties of Alumina–Tin Oxide Nanocomposites Deposited on 1*D* Carbon Backbone

Deepti R. Kulkarni[1], Narasimha H. Ayachit[1,2], Raviraj M. Kulkarni[3], and Suresh D. Kulkarni[4]

[1]*Department of Physics,*
Rani Channamma University,
591156 Belagavi, Karntaka, India
[2]*KLE Technological University, Vidya Nagar,*
580031 Hubballi, Karnataka, India
[3]*Centre for Nanoscience and Nanotechnology and Department of Chemistry,*
KLS Gogte Institute of Technology (Autonomous),
590008 Udyambag, Belagavi, Karnataka, India
[4]*Department of Atomic and Molecular Physics, MIT,*
Manipal Academy of Higher Education,
576104 Manipal, India

Alumina–tin oxide nanocomposites deposited on 1*D* carbon backbone for solar cell and optoelectronic applications are synthesized by simple co-precipitation method. The nanocomposites are characterized by different techniques. The TEM image indicates that the prepared Al_2O_3–SnO_2 nanocomposites are deposited on 1*D* carbon backbone. The length of the nanowire is in a few micrometers, and radius is of around 10 nm. The elemental analysis shows the presence of peaks due to Al, Sn, C and O. The average crystallite size of SnO_2 is found to be 5.185 nm from XRD analysis. Further, no peaks related Al_2O_3 are detected indicating amorphous phase of Al_2O_3 nanoparticles. Room-temperature photoluminescence spectroscopy of Sn–Al_2O_3 nanowires reveals emission ranging from 410 nm to 540 nm comprising of multiple emission bands centred at 433 and 504 nm and additionally shoulder peaks at 445, 455, 478 and 488 nm. None of these bands corresponds to the band-gap of the material and, hence, should be due to different defect states within the band-gap. UV–Visible diffused reflectance studies reveal that the band-gap of the nanocomposites is of 4.23 eV. BET investigation shows that the specific surface area of the nanocomposites is of 130 $m^2 \cdot g^{-1}$ and pore volume is of 0.268 $cm^3 \cdot g^{-1}$. The estimated high exciton-binding energy of alumina–tin oxide nanocomposites deposited on 1*D* carbon backbone is crucial in optoelectronic applications.

Нанокомпозити з глинозему й оксиду Стануму, яких осаджено на одновимірній вуглецевій опорі, для сонячних елементів і оптоелектронних застосувань синтезуються простою методою сумісного осадження. Нанокомпозити характеризуються різними методами. Зображення просвітлювальної електронної мікроскопії вказує на те, що підготовлені нанокомпозити Al_2O_3–SnO_2 осідають на одновимірній вуглецевій опорі. Довжина нанодроту становить кілька мікрометрів, а радіюс становить близько 10 нм. Елементна аналіза показує наявність піків за рахунок Al, Sn, C і O. Середній розмір кристалітів SnO_2 становить 5,185 нм за даними рентґенівської дифрактометричної аналізи. Крім того, не виявлено піків, пов'язаних з Al_2O_3, що вказує на аморфну фазу наночастинок Al_2O_3. За кімнатної температури спектроскопія фотолюмінесценції нанодротів Sn–Al_2O_3 виявляє емісію від 410 нм до 540 нм, що складається з декількох емісійних смуг, зосереджених на 433 і 504 нм, а також уступчасті піки при 445, 455, 478 і 488 нм. Жодна з цих смуг не відповідає забороненій (енергетичній) зоні матеріялу і, отже, має бути пов'язана з різними дефектними станами всередині забороненої (енергетичної) зони. Дослідження розсіяного відбивного відображення у видимій і ультрафіолетовій областях виявляють, що заборонена (енергетична) щілина нанокомпозитів становить 4,23 еВ. Дослідження за Брунауером, Емметом і Теллером показує, що питома площа поверхні нанокомпозитів становить 130 $м^2 \cdot г^{-1}$, а об'єм пор — 0,268 $см^3 \cdot г^{-1}$. За оцінками висока енергія екситонного зв'язування для нанокомпозитів з глинозему й оксиду Стануму, що осаджені на одновимірній вуглецевій опорі, має вирішальне значення в оптоелектронних застосуваннях.

Key words: alumina, tin oxide, 1*D* carbon backbone, band-gap, solar cells, optoelectronics.

Ключові слова: глинозем, оксид Стануму, одновимірна вуглецева опора, заборонена (енергетична) щілина, сонячні батареї, оптоелектроніка.

(Received 23 July, 2020; in revised form, 12 September, 2020)

1. INTRODUCTION

Semiconducting metal oxides have been comprehensively studied due to their extraordinary optoelectronic and structural properties, which are of technological significance [1, 2, 3, 4]. They demonstrate good electrical conductance and better transmittance in UV–Visible range. Hence, they find applications in the construction of solar cells and nanosheet transistors [5, 6]. The efficiency of solar cells and nanosheet transistors depends on the optoelectronic properties of the electrodes [7].

Dye-sensitized solar cells (DSSCs) and quantum dot-sensitized solar cells (QDSSCs) based on semiconductor electrodes are highly regarded as substitutes for conventionally used silicon-based photo-

voltaic cells, given the ease of fabrication, low-cost and eco-friendliness [8, 9].

A perfect photoanode for DSSCs/QDSSCs must possess characteristics such as large surface area, rapid electron transportation and low electron recombination [10, 11]. Many attempts have been made in the literature to develop SnO_2 photoanodes [12, 13]. Nanostructured tin oxide (SnO_2 NP) is *n*-type semiconductor having good structural and optoelectronic properties [14, 15]. SnO_2 NP and its composites find applications in photovoltaic cells, catalysis, gas sensors, antistatic coatings, transparent electrodes, *etc.* [16, 17, 18]. The transparent and conductive nature of SnO_2 NP is possibly due to deviations from stoichiometry, impurities and by the microstructures [19].

Aluminium oxide nanoparticles (Al_2O_3 NP) exhibit remarkable properties like large dielectric constant, wide band-gap, good corrosion resistance and good adherent to materials [20]. Al_2O_3 NP have recently emerged as an alternative passivation material [21, 22]. Al_2O_3 NP are utilized in variety of industries in the manufacture of catalysts, sensors, antireflection coatings, abrasive materials and nanolaminates.

Nanowires exhibit rapid electron transport in DSSCs compared to nanoparticles. This rapid electron transport in nanowires is due to the presence lesser number of grain boundaries, good contact and surface area [23, 24]. The nanowires offer direct electric route for swift collection of charges in DSSCs/QDSCs [20, 21].

In the present work, we have reported a simple single step co-precipitation technique to synthesize Al_2O_3–SnO_2 nanocomposites and deposited on 1*D* carbon backbone.

The main objective of this work is to study the optical, electronic, and structural properties of these nanocomposites for solar cells and other optoelectronic devices.

2. EXPERIMENTAL

The precursors used for the preparation of Al_2O_3–SnO_2 nanocomposite were $Al_2(SO_4)_3$, $SnCl_2$, polyethylene glycol (PEG 200) and ammonia (NH_3). All chemicals used were of analytical grade.

16.65 g of aluminium sulphate ($Al_2(SO_4)_3$) with 2.37 g of stannous chloride ($SnCl_2$) were dissolved in 100 ml distilled water. 3 g of polyethylene glycol (PEG 200) was added to the solution in order to prevent agglomeration of particles and precursor for carbon wire. Above-mentioned solution was titrated with drop wise addition of ammonia solution (30% conc.) and simultaneously stirred at 800 rpm using magnetic stirrer till the pH meter reads 9. The product formed is heated to 400°C for 3 hours and then washed

with ethanol and distilled water. Finally, the nanocomposites were calcined at 550°C.

Be means of reactions

$$Al_2(SO_4)_3 + 6NH_4OH \rightarrow Al_2O_3 \cdot 3H_2O + 3(NH_4)_2SO_4,$$

$$SnCl_2 + 2NH_4OH \rightarrow SnO \cdot H_2O + 2NH_4Cl,$$

during calcination, SnO_2 is formed:

$$SnO \cdot H_2O + 0.5O_2 \rightarrow SnO_2 + H_2O.$$

Transmission electron microscopy, energy-dispersive x-ray, scanning electron microscopy, x-ray diffraction, BET surface area and UV–Vis diffused reflectance techniques were used to characterize Al_2O_3–SnO_2 nanocomposite on 1*D* carbon backbone.

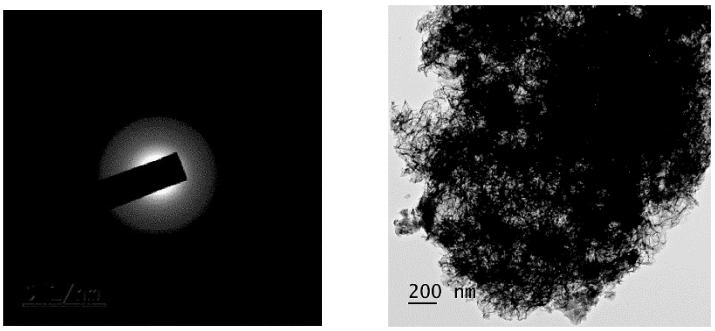

Fig. 1. SAED and TEM image of Al_2O_3–SnO_2 nanocomposites on carbon nanowire.

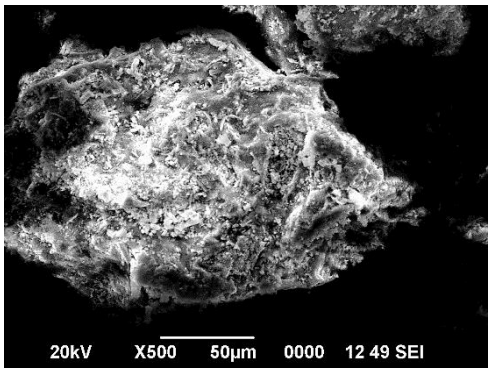

Fig. 2. SEM image of Al_2O_3–SnO_2 nanocomposites on carbon nanowire.

3. RESULTS AND DISCUSSIONS

The transmission electron microscopy image indicates that the prepared Al_2O_3–SnO_2 nanocomposites were deposited on 1*D* carbon backbone. The length of the nanowire was in a few micrometers, and radius was of around 10 nm. After observing SAED image (Fig. 1), it was clear that bright spots are not visible because particle sizes were very small, and it was in the form of continuum addition to that, amorphous Al_2O_3 covered the crystalline SnO_2 particles.

Figure 2 shows the SEM image of Al_2O_3–SnO_2 nanocomposites on 1*D* carbon backbone taken with JEOL JSM-6360 model. The SEM reveals the spongy and porous structure of agglomerated Al_2O_3–SnO_2 nanocomposites on 1*D* carbon backbone. These nanostructures have diverse shapes and sizes, which lead to a better surface area. The SEM image reveals that the agglomerated particles were closely packed having irregular shape. This indicates that the nanowires were entangled.

The XRD analysis (Fig. 3) of Sn-doped Al_2O_3 nanoparticle shows the characteristic diffraction peaks of SnO_2, but no peaks of Al_2O_3. This is because Al_2O_3 formed is amorphous in nature, whereas SnO_2 is in crystalline form. The positions of peaks (planes) at 26.576 (100), 33.379 (101), 37.501 (200), 51.502 (211), 65.398 (301) confirm the rutile-type tetragonal phase of SnO_2. The XRD peaks are of relatively lower intensity as compared to standard SnO_2. This is because crystalline SnO_2 particles are trapped inside the amorphous Al_2O_3.

The average crystallite size of 5.185 nm for SnO_2 was obtained from Debye–Scherrer equation. The small size of SnO_2 is because of addition of excess PEG as a precursor for 1*D* carbon backbone is also acting as a capping agent during preparation [25].

The EDX analysis of Al_2O_3–SnO_2 composite on 1*D* carbon back-

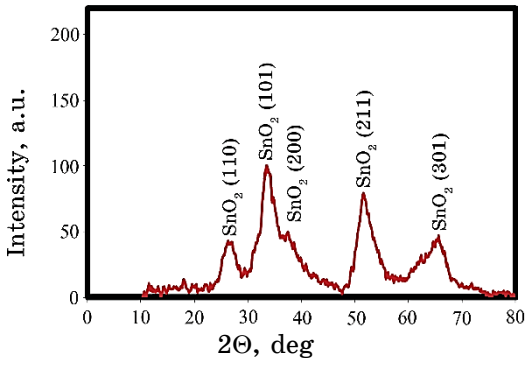

Fig. 3. XRD of Al_2O_3–SnO_2 nanocomposites on carbon nanowire.

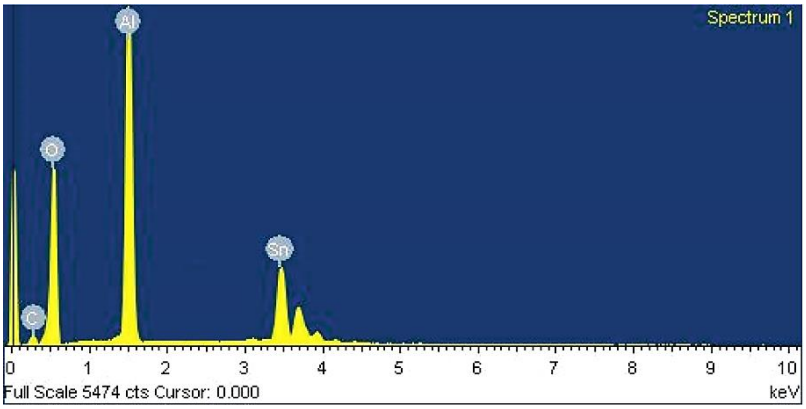

Fig. 4. EDX of Al_2O_3–SnO_2 nanocomposites on carbon nanowire.

TABLE. Specific surface area and pore volume of Al_2O_3–SnO_2 nanocomposites on carbon.

Sample	Specific surface area, $m^2 \cdot g^{-1}$	Pore volume, $cm^3 \cdot g^{-1}$
Al_2O_3–SnO_2 nanocomposite on 1*D* carbon backbone	130.4	0.268

bone (Fig. 4) was achieved with the JEOL JED-2300 instrument. It confirms the occurrence of four separate x-ray peaks belonging to C, O, Al and Sn. The energy-dispersive x-ray analysis indicates the existence of peaks related to Al, Sn, C and O.

BET nitrogen gas adsorption method (SmartSorb 92/93) was used to measure the specific surface area of nanocomposites. The specific surface area and pore volume of nanocomposites are given in Table.

UV–Visible diffused reflectance spectroscopy is a standard method in the evaluation of the absorption characteristics of nanostructures. Energy band-gap and absorption coefficient are the essential properties of nanostructures for optoelectronic applications and are estimated by means of the diffused reflectance spectroscopy.

The diffuse reflectance spectra of nanocomposites (Fig. 5) were collected using a UV/Vis/NIR spectrophotometer equipped with a 150 mm integrating sphere using $BaSO_4$ as a reflectance standard. The Kubelka–Munk theory was used to transform diffused reflectance measurements (R_∞) to absorption coefficient α:

$$\alpha \approx \frac{k}{S} = \frac{(1 - R_\infty)^2}{2R_\infty} \equiv f_{\text{KM}}(R_\infty) .$$

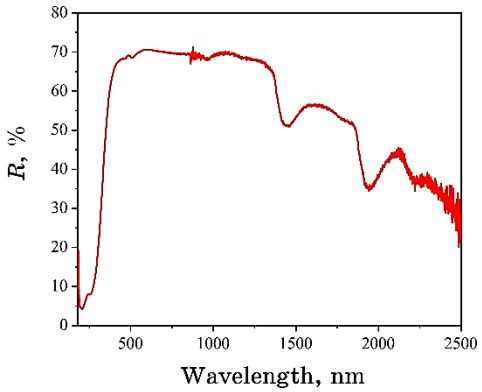

Fig. 5. The diffused reflectance spectra of Al_2O_3–SnO_2 nanocomposites deposited on 1*D* carbon backbone.

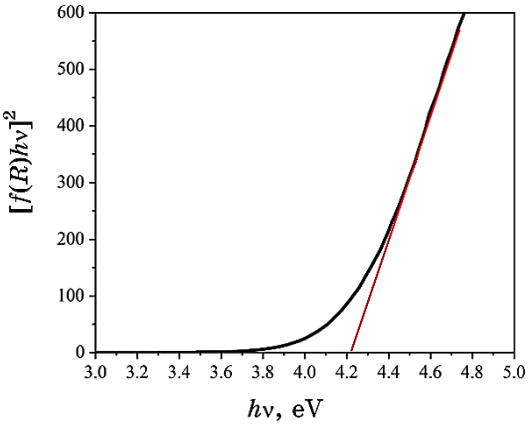

Fig. 6. The Tauc plot for determining the band-gap of alumina–tin oxide composite deposited on 1*D* carbon backbone.

Here, $f_{KM}(R_\infty)$ is the Kubelka–Munk (KM) function, whereas k and S are absorption and scattering coefficients, respectively. For the direct transition, band-gap E_g of nanocomposites was evaluated by the Tauc method that is expressed as

$$(\alpha h\nu) = A\left(h\nu - E_g\right)^{1/2},$$

where A is a constant, which depends on the wavelength, h and ν are Planck's constant and frequency, respectively [26].

Tauc plot of KM function was used to asses optical band-gap of Al_2O_3–SnO_2 nanocomposites deposited on 1*D* carbon backbone (Fig. 6). E_g was obtained by extending the linear portion of $[f_{KM}(R_\infty)h\nu]^{1/2}$

vs the photon energy ($h\nu$) curve on the zero ordinate. The band-gap of the alumina–tin oxide nanocomposites on 1*D* carbon backbone is of 4.23 eV.

Filatova *et al.* reported [27] the band-gap of 7.0 eV for amorphous Al_2O_3 and 7.6 eV for γ-Al_2O_3. Toyoda *et al.* reported [28] the band-gap of 5.1–7.1 eV for Al_2O_3 nanofilms. The variation in the band-gap is primarily attributed to shift in the location of lower edge of conduction band. The movement of electrons from aluminium to oxygen atom controls the location of conduction band. Al atom coordination symmetry governs the charge transfer process.

The room-temperature photoluminescence excitation and emission spectra were collected by means of Jasco FP8300 photoluminescence spectrometer. The instrument is attached with xenon light source and a high-speed chopper.

Room-temperature photoluminescence spectroscopy of Al_2O_3–SnO_2 on 1*D* carbon backbone (Fig. 7) revealed emission ranging from 410 nm to 540 nm comprising of multiple emission bands centred at 433 and 504 nm and additionally shoulder peaks at 445, 455, 478 and 488 nm. None of these bands corresponds to the band-gap of Al_2O_3 or SnO_2 and, hence, should be due to various defect states within the band-gap.

The observed emission bands may be due to SnO_2 formed at the annealing temperature of 550–600°C. Similar emissions were observed with the SnO_2 nanoribbons [29].

Generally, oxygen vacancies in oxides serve as luminescence centres apart from other possible defects. Tin vacancies or tin interstitials may also form trapped states within the band-gap [30, 31, 32, 33, 34].

Wide band-gap and high exciton-binding energy make any semi-

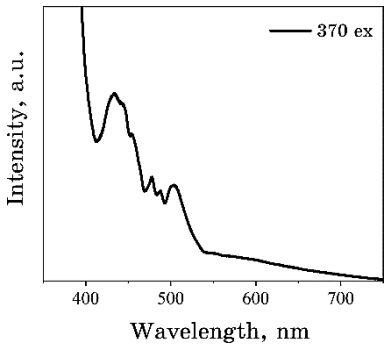

Fig. 7. Room-temperature photoluminescence spectroscopy of Al_2O_3–SnO_2 on 1*D* carbon backbone.

conductor suitable for optoelectronic-device applications such as window layer for solar cells. Excitons are electron–hole pairs, which are generated when photon strikes semiconductor nanostructures. The thermal and electron transport properties are important to photovoltaic systems. The parting of exciton into a free electron and free hole is the source of electrical energy in a dye-sensitized solar cell. The diffusion of excitons to an interface that can then divide them into electrons and holes remains a central challenge in many photovoltaics. An attempt has been made to estimate the exciton-binding energy for alumina–tin oxide nanocomposite on 1*D* carbon backbone. Photoluminescence is fundamentally the recombination of exciton, during which excited electron go back to the valence band. Photoluminescence line is the difference between the band-gap and exciton-binding energy $(E_g - E_{ex})$ [35]. The band-gap of 4.23 eV for alumina–tin oxide nanocomposite was determined by UV–Visible diffused reflectance spectroscopy. Exciton-binding energy $\approx 4.2 - 3.0 = 1.2$ eV. These extremely high exciton-binding energies mean that excitonic behaviour dominates at room temperature and above, and we are indeed able to follow the evolution of these characteristics to 300 K [36]. Due to the large exciton-binding energy, the true band-gap is substantially higher than the dominant spectral characteristic normally observed with photoluminescence [37, 38]. This information is crucial for developing future technological applications and enables further progress in both experimental and theoretical efforts to understand better alumina–tin oxide nanocomposite on 1*D* carbon backbone.

4. CONCLUSIONS

Alumina–tin oxide nanocomposites deposited on 1*D* carbon backbone were synthesized by simple precipitation technique. The nanocomposites were characterized by electron microscopy and x-ray diffraction techniques. The crystalline phase of tin oxide is rutile-type tetragonal, and alumina is amorphous. The optical band-gap of the composite is of 4.23 eV. The photoluminescence property of the nanocomposites may be due to tin or oxygen vacancies. The estimated high exciton-binding energy of alumina–tin oxide nanocomposites deposited on 1*D* carbon backbone is crucial in optoelectronic applications.

REFERENCES

1. R. Kumaravel, V. Krishnakumar, V. Gokulakrishnan, K. Ramamurthi, and K. Jeganathan, *Thin Solid Films*, **518**, Iss. 8: 2271 (2010);

https://doi.org/10.1016/j.tsf.2009.08.049
2. D. Liu, S. Ren, X. Ma, C. Liu, L. Wu, W. Li, J. Zhang, and L. Feng, *RSC Adv.*, **7**, Iss. 14: 8295 (2017); https://doi.org/10.1039/C6RA27146D
3. C. Messaadi, M. Ghrib, H. Chenaina, M. Manso-Silván and H. Ezzaouia, *J. Mater. Sci.: Mater. Electron.*, **29**, Iss. 4: 3095 (2018); https://doi.org/10.1007/s10854-017-8241-3
4. S. Dinesh, M. Anandan, V.K. Premkumar, S. Barathan, G. Sivakumar, and N. Anandhan, *Mater. Sci. Eng. B*, **214**: 37 (2016); https://doi.org/10.1016/j.mseb.2016.08.006
5. K. Han, M. Xie, L. Zhang, L.Yan, J. Wei, G. Ji, Q. Luo, J. Lin, Y. Hao, and C.-Q. Ma, *Sol. Energy Mater. Sol. Cells*, **185**: 399 (2018); https://doi.org/10.1016/j.solmat.2018.05.048
6. F. F. Vidor, T. Meyers, G. I. Wirth, and U. Hilleringmann, *Microelectron. Eng.*, **159**: 155 (2016); https://doi.org/10.1016/j.mee.2016.02.059
7. N. K. Mishra, C. Kumar, A. Kumar, M. Kumar, P. Chaudhary, and R. Singh, *Mater. Sci.–Poland*, **33**, Iss. 4: 714 (2015); https://doi.org/10.1515/msp-2015-0101
8. D. Wang, S. Liu, M. Shao, Q. Li, Y. Gu, J. Zhao, X. Zhang, J. Zhao, and Y. Fang, *Ind. Eng. Chem. Res.*, **57**, Iss. 21: 7136 (2018); https://doi.org/10.1021/acs.iecr.8b00039
9. Z. Pan, H. Rao, I. Mora-Sery, J. Bisquert, and X. Zhong, *Chem. Soc. Rev.* **47**, Iss. 20: 7659 (2018); https://doi.org/10.1039/C8CS00431E
10. X. Mao, R. Zhou, S. Zhang, L. Ding, L. Wan, S. Qin, Z. Chen, J. Xu, and S. Miao, *Sci. Rep.*, **6**: 19390 (2016); https://doi.org/10.1038/srep19390
11. C. Gao, X. Li, B. Lu, L. Chen, Y. Wang, F. Teng, J. Wang, Z. Zhang, X. Pan, and E. Xie, *Nanoscale*, **4**, Iss. 11: 3475 (2012); https://doi.org/10.1039/C2NR30349C
12. B. Liu, L. Wang, Y. Zhu, Y. Xia, W. Huang, and Z. Li, *Electrochim. Acta*, **295**: 130 (2019); https://doi.org/10.1016/j.electacta.2018.10.129
13. H. M. A. Javed, W. Que, X. Yin, L. B. Kong, J. Iqbal, and M. S. Mustafa, *Mater. Res. Bull.*, **109**: 21 (2019); https://doi.org/10.1016/j.materresbull.2018.09.016
14. Y. Zhou, W. Xu, S. Lv, C. Yin, J. Li, B. Zhu, Y. Liu, and C. He, *J. Alloys Compd.*, **732**: 555 (2018); https://doi.org/10.1016/j.jallcom.2017.10.234
15. S. Dabbabi, T. B. Nasr, S. Ammar, and N. Kamoun, *Superlattices and Microstruct.*, **123**: 129 (2018); https://doi.org/10.1016/j.spmi.2018.05.058
16. T. Toupance, O. Babot, B. Jousseaume, and G. Vilaca, *Chem. Mater.*, **15**, Iss. 24: 4691 (2003); https://doi.org/10.1021/cm0344459
17. S. Das and V. Jayaraman, *Prog. Mater. Sci.*, **66**: 112 (2014); https://doi.org/10.1016/j.pmatsci.2014.06.003
18. K. Gotlib-Vainstein, I. Gouzman, O. Girshevitz, A. Bolker, N. Atar, E. Grossman, and C. N. Sukenik, *ACS Appl. Mater. Interfaces*, **7**, Iss. 6: 3539 (2015); https://doi.org/10.1021/am5072817
19. Y. S. Jung and S. S. Lee, *J. Cryst. Growth*, **259**, Iss. 4: 343 (2003); https://doi.org/10.1016/j.jcrysgro.2003.07.006
20. M. H. Boratto, L. V. de Andrade Scalvi, J. L. B. Maciel Jr., M. J. Saeki, and E. A. Floriano, *Materials Research*, **17**, Iss. 6: 1420 (2014); http://dx.doi.org/10.1590/1516-1439.285114

21. G. He, J. Gao, H. Chen, J. Cui, Z. Sun, and X. Chen, *ACS Appl. Mater. Interfaces*, **6**, Iss. 24: 22013 (2014); https://doi.org/10.1021/am506351u
22. Y. J. Kim, S. M. Kim, S. Heo, H. Lee, H. I. Lee, K. E. Chang, and B. H. Lee, *Nanotechnology*, **29**, Iss. 5: 055202 (2018); https://doi.org/10.1088/1361-6528/aaa0e2
23. X. Cao, Q. He, W. Shi, B. Li, Z. Zeng, Y. Shi, Q. Yan, and H. Zhang, *Small*, **7**, Iss. 9: 1199 (2011); https://doi.org/10.1002/smll.201100071
24. Z. Salam, E. Vijayakumar, and A. Subramania, *RSC Adv.*, **4**, Iss. 95: 52871 (2014); https://doi.org/10.1039/C4RA09151E
25. S. Cholan, N. Shanmugam, N. Kannadasan, K. Sathishkumar, and K. Deivam, *J. Mater. Res. Technol.*, **3**, Iss. 3: 222 (2014); https://doi.org/10.1016/j.jmrt.2014.04.001
26. M. Karmaoui, A. B. Jorge, P. F. McMillan, A. E. Aliev, R. C. Pullar, J. A. Labrincha, and D. M. Tobaldi, *ACS Omega*, **3**, Iss. 10: 13227 (2018); https://doi.org/10.1021/acsomega.8b02122
27. E. O. Filatova and A. S. Konashuk, *J. Phys. Chem. C*, **119**, Iss. 35: 20755 (2015); https://doi.org/10.1021/acs.jpcc.5b06843
28. S. Toyoda, T. Shinohara, H. Kumigashira, M. Oshima, and Y. Kato, *Appl. Phys. Lett.*, **101**, Iss. 23: 231607 (2012); https://doi.org/10.1063/1.4769818
29. J. Q. Hu, X. L. Ma, N. G. Shang, Z. Y. Xie, N. B. Wong, C. S. Lee, and S. T. Lee, *J. Phys. Chem. B*, **106**, Iss. 15: 3823 (2002); https://doi.org/10.1021/jp0125552
30. D. Calestani, L. Lazzarini, G. Salviati, and M. Zha, *Cryst. Res. Technol.*, **40**: 937 (2005); https://doi.org/10.1002/crat.200410463
31. J. H. He, T. H. Wu, C. L. Hsin, K. M. Li, L. J. Chen, Y. L. Chueh, L. J. Chou, and Z. L. Wang, *Small.*, **2**, Iss. 1: 116 (2006); https://doi.org/10.1002/smll.200500210
32. S. Brovelli, N. Chiodini, F. Meinardi, A. Lauria, and A. Paleari, *Appl. Phys. Lett.*, **89**, Iss. 15: 153126 (2006); https://doi.org/10.1063/1.2362583
33. F. Gu, S. F. Wang, C. F. Song, M. K. Lu, Y. X. Qi, G. J. Zhou, D. Xu, and D. R. Yuan, *Chem. Phys. Lett.*, **372**, Iss. 3: 451 (2003); https://doi.org/10.1016/S0009-2614(03)00440-8
34. F. Gu, S. F. Wang, M. K. Lü, G. J. Zhou, D. Xu, and D. R. Yuan, *J. Phys. Chem. B*, **108**, Iss. 24: 8119 (2004); https://doi.org/10.1021/jp036741e
35. Z. Jiang, Z. Liu, Y. Li, and W. Duan, *Phys. Rev. Lett.*, **118**, Iss. 26: 266401 (2017); https://doi.org/10.1103/PhysRevLett.118.266401
36. A. T. Hanbicki, M. Currie, G. Kioseoglou, A. L. Friedman, and B. T. Jonker, *Solid State Commun.*, **203**: 16 (2015); https://doi.org/10.1016/j.ssc.2014.11.005
37. T. Cheiwchanchamnangij and W. R. L. Lambrecht, *Phys. Rev. B*, **85**, Iss. 20: 205302 (2012); https://doi.org/10.1103/PhysRevB.85.205302
38. A. Ramasubramaniam, *Phys. Rev. B*, **86**, Iss. 11: 115409 (2012); https://doi.org/10.1103/PhysRevB.86.115409